Near-IR Absorption and Photocurrent Generation Using a First-of-Its-Kind Boron Difluoride Formazanate Non-Fullerene Acceptor

Josh D. B. Koenig[a], Mahmoud E. Farahat[a], Jasveer S. Dhindsa[b], Joe B. Gilroy*[b], and Gregory C. Welch*[a]

––––

[a] Department of Chemistry, University of Calgary, Calgary, Alberta, Canada T2N 1N4.

[b] Department of Chemistry and the Centre for Advanced Materials and Biomaterials Research (CAMBR), The University of Western Ontario, London, ON, Canada N6A 5B7.

––––

* Corresponding Authors:

Email: joe.gilroy@uwo.ca;
Phone Number: 1-519-661-2111 (ext. 81561)

Email: gregory.welch@ucalgary.ca;
Phone number: 1-403-210-7603

▪ Abstract

Herein, we report the synthesis and characterization of the first non-fullerene acceptor (NFA) containing a boron difluoride formazanate (**BF$_2$fz**) core end-capped with N-annulated perylene diimides (PDIs). Electronic coupling between the **BF$_2$fz** core and the PDI endcaps enabled tuning of the lowest unoccupied molecular orbital, leading to near-panchromatic optical absorption. Post-deposition solvent vapor annealing of the new NFA resulted in a significant red-shift in the optical spectra, which stretched into the near-IR. Proof-of-concept organic photovoltaic (OPV) devices were constructed to demonstrate the potential of this new material as an NFA. SVA treatment of the active layer resulted in a 2-fold increase in power conversion efficiency (PCE), due mainly to increases in the **BF$_2$PDI$_2$** generated photocurrent that extended into the near-IR.

▪ Introduction

For applications in organic photovoltaics (OPVs), π-conjugated materials are perfectly suited for use as non-fullerene acceptors (NFAs) because both physical and optoelectronic properties may be optimized to match the electron-donor material with which they are paired in the active layer.[1,2] One class of non-fullerene acceptors (NFAs) recognized for high redox and thermal stability, as well as high molar absorptivity, are perylene diimides (PDIs).[3,4] Despite such favorable qualities, the efficiency of charge-extraction for PDI-based NFA materials is often hindered by the formation of large π-π stacking domains throughout the BHJ.[1] To promote more favorable phase separation in the BHJ, PDI self-assembly may be disrupted through either direct dimerization of PDIs[5–7] or insertion of a core between the PDI-moieties.[8–19]
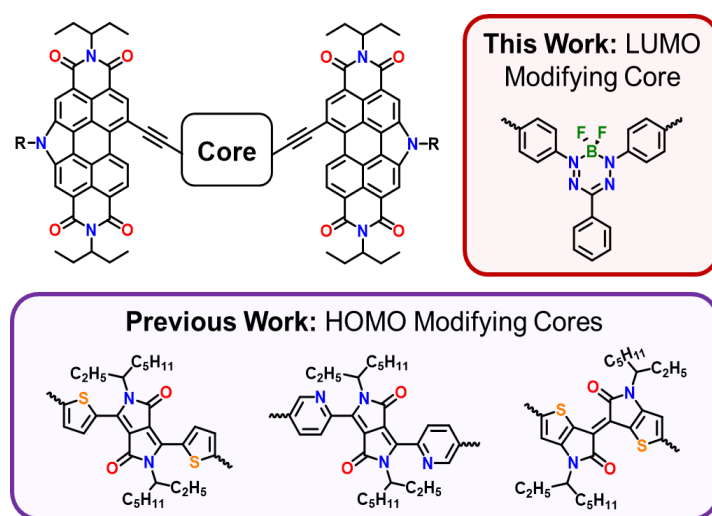

Fig. 1 Depicting previously investigated HOMO-modifying and newly synthesized LUMO-modifying N-annulated PDI-core-PDI materials.

Our research group has previously explored the optoelectronic influence of thienoisoindigo, thienyl- and pyridyl- diketopyrrolopyrrole cores that were acetylene-linked to N-annulated PDI (Fig. 1).[20] Strong electronic communication between the cores and PDI endcaps adjusted the highest occupied molecular orbital (HOMO) energy level of these molecules, affording near-panchromatic absorptions ideally suited for OPV. In search of a core that could achieve similar absorptivity, while instead influencing the lowest unoccupied molecular (LUMO) energy level, we targeted an acetylene-terminated boron difluoride formazanate (**BF₂fz**).[21–23] The properties of **BF₂fz** materials are highly sensitive to structural variation at the N-aryl substituents,[24–26] meaning the optoelectronic properties can be tuned by the choice of endcap material. In this contribution, we report the synthesis, characterization, and NFA capability of a new π-conjugated material comprised of a **BF₂fz** core acetylene-linked to N-annulated PDI endcaps (**BF₂PDI₂**).

- **Characterization**

The **BF₂fz** core and N-annulated PDI end caps were connected *via* a Sonogashira cross-coupling reaction to generate **BF₂PDI₂** (see Supporting Information for full experimental details). The identity of **BF₂PDI₂** was confirmed by ^{1}H, ^{11}B, ^{13}C, and ^{19}F NMR spectroscopy, as well as MALDI TOF mass spectrometry and CHN elemental analysis (Figs. S1-7). The ^{11}B and ^{19}F NMR spectra exhibited diagnostic 1:2:1 triplet and 1:1:1:1 quartet coupling patterns, respectively.[24] Moreover, the ^{1}H NMR spectrum showed no evidence of a formazan related N-H peak (at ~15 ppm),[21] strongly suggesting the **BF₂fz** core remained intact throughout synthesis and purification.

The thermal properties of **BF₂PDI₂** were measured using a combination of differential scanning calorimetry and thermal gravimetric analysis (Figs. S8-9). No obvious glass transitions or melting points were observed between 100 - 300 °C, while the onset of molecular decomposition was not observed until >300 °C. The high thermal stability observed in **BF₂PDI₂** may be attributed to significant π-conjugation between the **BF₂fz** core and the N-annulated PDI endcaps. This notion was supported by the density functional theory (DFT) optimized structure of **BF₂PDI₂** at the B3LYP-6-31G(d,p) level of theory (Fig. S13). The PDI units were nearly co-planar with each other, with only a small degree of bending caused by the **BF₂fz** core. This DFT optimized 'dragonfly' structure corresponded well with previously determined X-ray crystallography structures for compounds using the same **BF₂fz** core.[22,23]
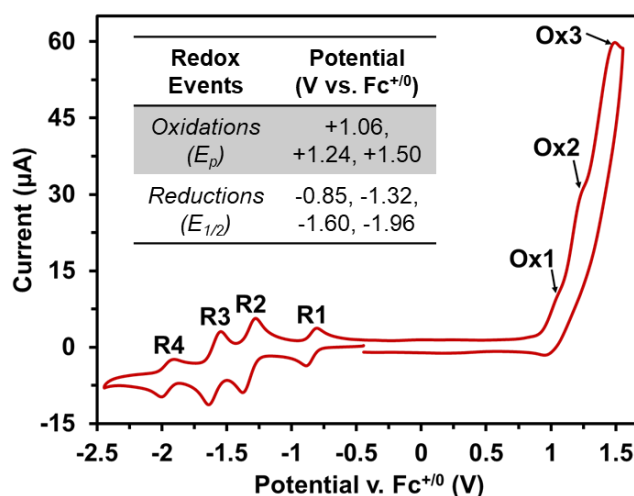

Fig. 2 Cyclic voltammogram of BF₂PDI₂, measured at 100 mV/s in CH₂Cl₂ under argon with 0.1 M TBAPF₆ supporting electrolyte (WE = glassy carbon, CE = Pt-wire, *pseudo*-RE = Ag/AgCl). Inset are all measured oxidation (Ox) and reduction (R) events, referenced to Fc⁺/⁰.

Next, the electronic properties of **BF₂PDI₂** were probed using cyclic voltammetry (CV), with additional information provided by DFT calculations. The CV of **BF₂PDI₂** was comprised of three irreversible oxidation events, as well as four fully reversible reduction events (Fig. 2). While the number oxidation events could be determined by differential pulse voltammetry (Fig. S12), the precise electrochemical origin may not be readily assigned. On the other hand, the first and fourth

reductions ($E_{1/2}$ = -0.85 and -1.96 V vs. Fc$^{+/0}$) may be attributed to **BF₂fz** core, while the second and third reduction events ($E_{1/2}$ = -1.32 and -1.60 V vs. Fc$^{+/0}$) may be attributed to N-annulated PDI as the current passed during these redox processes was 2x larger. By DFT calculations, the first oxidation event appeared to be delocalized across the entire molecule, while the first reduction event was largely centered on the **BF₂fz** core (Fig. S14). These predicted HOMO-LUMO energy levels correlate well with the observed CV data. Together, these data strongly suggest that the **BF₂fz** core has a higher electron affinity than the N-annulated PDI endcaps, which served to lower the LUMO energy level of **BF₂PDI₂**, when compared to related compounds with different cores.[20]

The optical properties of **BF₂PDI₂** were measured by UV-visible-nearIR absorption spectroscopy (UV-vis-nIR). The UV-vis-nIR profile of **BF₂PDI₂** in solution possessed a broad absorbance between 450 - 750 nm, with an absorption maximum (λ_{max}) at 543 nm attributable to the PDI endcaps (Fig. 3). When spin-cast into a thin-film, the optical profile of **BF₂PDI₂** underwent several notable changes. Beyond the slightly red-shifted onset of absorption (λ_{onset}), the broadening of λ_{max} was also accompanied by an appreciable increase in the intensity of the low-energy intramolecular charge transfer (ICT) band.[20]
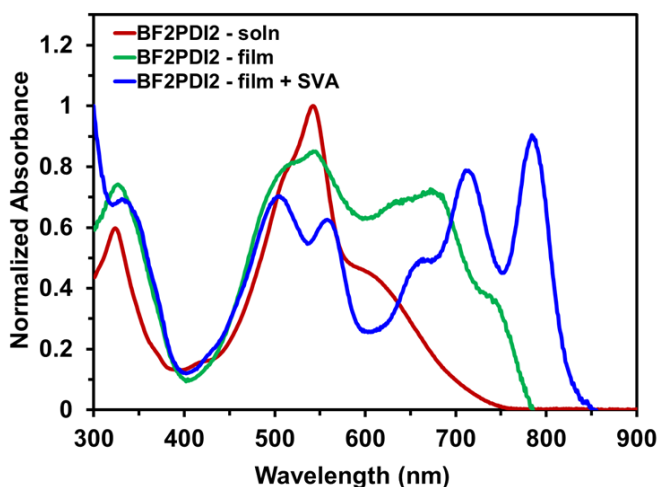

Fig. 3 UV-vis absorption profile of BF₂PDI₂ in CHCl₃ solution (red), thin-film spin-cast from *o*-dichlorobenzene (green), and the same thin-film solvent vapor annealed from CHCl₃ (blue).

In the past, we have shown that post-deposition solvent vapor annealing (SVA) can induce structural order within the solid-state morphology of similar PDI-core-PDI materials.[10,27–30] Exposure of this thin-film to CHCl₃ solvent vapors caused the once broad solid-state optical profile to resolve into two distinct absorption regions. The PDI-based λ_{max} region was split into two peaks (λ = 508 and 560 nm), while the low-energy ICT shoulder developed fine structure (λ_{max} = 790 nm) that extended well into the near-IR (λ_{onset} = 850 nm). This behaviour is strongly indicative of reorganization and/or aggregation of **BF₂PDI₂** into more ordered domains in the solid-state.[31–33]

- **OPV Devices**

The NFA capabilities of **BF$_2$PDI$_2$** were assessed by constructing some proof-of-concept OPV devices with the following inverted architecture: ITO/ZnO/Ternary Active Layer/MoOx/Ag (full experimental details in SI). A ternary active layer comprised of electron-donor polymer PPDT2FBT (FBT), PC$_{61}$BM, and **BF$_2$PDI$_2$** was employed for OPV devices. FBT was selected because of its complementary absorption with the solvent vapor annealed **BF$_2$PDI$_2$** (Fig. S15). PC$_{61}$BM was added to this ternary blend to assist with charge mobility.[34] Using an initial FBT:**BF$_2$PDI$_2$**:PC$_{61}$BM blend ratio of (1:1:0.5) at 10 mg/mL total concentration, the OPV devices achieved a open circuit voltage (V_{oc}) of 0.69 V, a short circuit current (J_{sc}) of 1.1 mA/cm^2, and a fill factor (FF) of 41 %, leading to a power conversion efficiency (PCE) of 0.3 %.

Post-deposition treatment of these films with CHCl$_3$ SVA resulted in the desired optical profile shift of **BF$_2$PDI$_2$**, giving the OPV devices a near-panchromatic absorbance (Fig. 4A). Device performance was maximized after 5 mins of CHCl$_3$ SVA, where both the J_{sc} and FF increased to 1.9 mA/cm^2 and 49 %, respectively, leading to a 2-fold increase in PCE to 0.6 % (Fig. 4B). Longer SVA treatments led to OPV performances similar to as-cast devices (Fig. S16 and Table S2). This phenomena has previously been observed with our N-annulated PDI-core-PDI materials and was attributed to over-annealing of the active layer.[10,27] Further attempts to optimize the ternary blend by altering the FBT:**BF$_2$PDI$_2$**:PC$_{61}$BM ratio and/or increasing total concentration were found to improve as-cast devices (Fig. S17 and Table S3). However, following SVA treatment of these devices, overall OPV performance was negatively impacted.
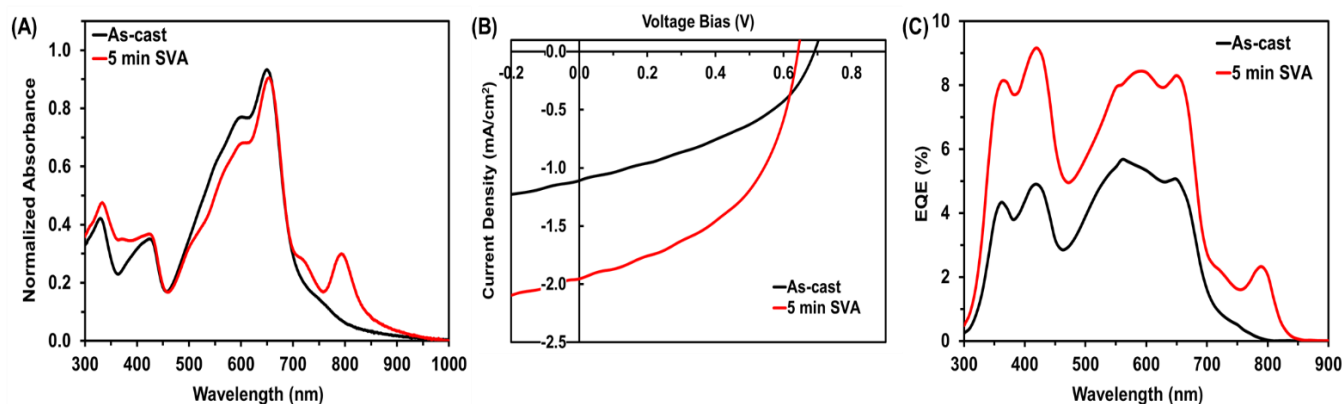
Fig. 4 Optical absorption profile (A), J-V curves (B), an external quantum efficiency plots (C) comparing the effects of solvent vapor annealing on ternary blend OPV devices with a FBT:BF$_2$PDI$_2$:PC$_{61}$BM (1:1:0.5) active layer at 10 mg/mL total concentration.

To better understand the observed enhancement in OPV performance for FBT:**BF$_2$PDI$_2$**:PC$_{61}$BM (1:1:0.5) ternary blends that were solvent vapor annealed from CHCl$_3$ for 5 min, photoluminescence (PL) and external quantum efficiency (EQE) experiments were performed. PL measurements of the ternary blend showed efficient quenching of the FBT polymer before and

after SVA treatment (Fig. S18). Analysis of the EQE spectra, the measured photocurrent clearly displays contributions from all components of the ternary blend (Fig. 4C). Following SVA treatment, photocurrent generation was extended well into the near-IR (λ_{max} = 790 nm), clearly emphasizing the increased contribution from the new NFA material, **BF₂PDI₂**.
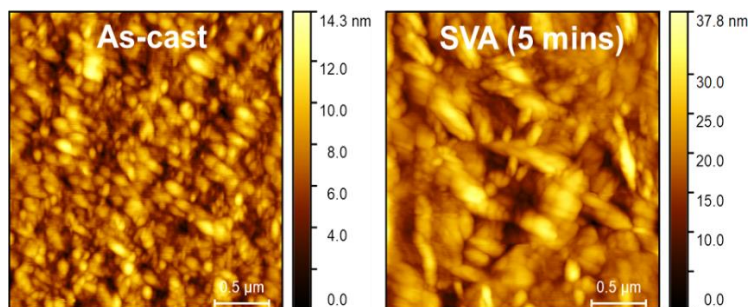
Fig. 5 Atomic force microscopy height images of ternary blend OPV devices with an FBT:BF$_2$PDI$_2$:PC$_{61}$BM (1:1:0.5) active layer at 10 mg/mL total concentration.

Surface morphology differences between the as-cast and SVA treated devices were also monitored by atomic force microscopy (AFM). AFM height images showed significant differences between the as-cast and SVA treated devices (Fig. 5), as the root-mean square surface roughness of the films increased from 1.9 nm to 4.8 nm. X-ray diffraction (XRD) measurements of ternary blend films before and after CHCl$_3$ SVA failed to show any distinguishing features that could be attributed to **BF₂PDI₂** (Fig. S19).[35] Together, these data strongly suggest that SVA enhanced OPV performance by inducing favorable **BF₂PDI₂** aggregation, rather than self-assembly into crystalline domains.[27,31–33]

▪ **Conclusions**

In conclusion, we have synthesized and fully characterized a first-of-its-kind NFA containing a **BF₂fz** core. The use of acetylene-linkers enabled through-conjugation between the **BF₂fz** core and the PDI endcaps, leading to an altered LUMO energy level that resulted in near-panchromatic absorption for **BF₂PDI₂**. Treatment of solid-state **BF₂PDI₂** with CHCl$_3$ SVA resulted in a significant bathochromic shift of the optical spectra, leading to near-IR absorption. The overall performance in a series of proof-of-concept OPV devices, where BF$_2$PDI$_2$ was used as an NFA in the ternary blend, was improved 2-fold by SVA treatment of the active layer. The increase in PCE could be mainly attributed to favorable aggregation of **BF₂PDI₂** in the active layer which increased the generated photocurrent. This notion was supported by EQE and AFM measurements. This work demonstrates the utility of the **BF₂fz** organic dye to construct narrow bandgap π-conjugated materials for use in organic electronics and provides the groundwork for further development.

▪ Acknowledgements

▪ References

1   S. Rajaram, R. Shivanna, S. K. Kandappa and K. S. Narayan, *J. Phys. Chem. Lett.*, 2012, **3**, 2405–2408.
2   C. B. Nielsen, S. Holliday, H.-Y. Chen, S. J. Cryer and I. McCulloch, *Acc. Chem. Res.*, 2015, **48**, 2803–2812.
3   Z. Liu, Y. Wu, Q. Zhang and X. Gao, *J. Mater. Chem. A*, 2016, **4**, 17604–17622.
4   W. Chen and Q. Zhang, *J. Mater. Chem. C*, 2017, **5**, 1275–1302.
5   D. Sun, D. Meng, Y. Cai, B. Fan, Y. Li, W. Jiang, L. Huo, Y. Sun and Z. Wang, *J. Am. Chem. Soc.*, 2015, **137**, 11156–11162.
6   D. Meng, D. Sun, C. Zhong, T. Liu, B. Fan, L. Huo, Y. Li, W. Jiang, H. Choi, T. Kim, J. Y. Kim, Y. Sun, Z. Wang and A. J. Heeger, *J. Am. Chem. Soc.*, 2016, **138**, 375–380.
7   A. D. Hendsbee, J.-P. Sun, W. K. Law, H. Yan, I. G. Hill, D. M. Spasyuk and G. C. Welch, *Chem. Mater.*, 2016, **28**, 7098–7109.
8   Y. Lin, Y. Wang, J. Wang, J. Hou, Y. Li, D. Zhu and X. Zhan, *Adv. Mater.*, 2014, **26**, 5137–5142.
9   Y. Duan, X. Xu, H. Yan, W. Wu, Z. Li and Q. Peng, *Adv. Mater.*, 2017, **29**, 1605115.
10   S. M. McAfee, S. V. Dayneko, P. Josse, P. Blanchard, C. Cabanetos and G. C. Welch, *Chem. Mater.*, 2017, **29**, 1309–1314.
11   J. Liu, S. Xie, S. Feng, M. Li, L. Wu, X. Xu, X. Chen, C. Li and Z. Bo, *J. Mater. Chem. C*, 2018, **6**, 9336–9340.
12   H. Lin, S. Chen, H. Hu, L. Zhang, T. Ma, J. Y. L. Lai, Z. Li, A. Qin, X. Huang, B. Tang and H. Yan, *Adv. Mater.*, 2016, **28**, 8546–8551.
13   Q. Wu, D. Zhao, A. M. Schneider, W. Chen and L. Yu, *J. Am. Chem. Soc.*, 2016, **138**, 7248–7251.
14   J. Zhang, Y. Li, J. Huang, H. Hu, G. Zhang, T. Ma, P. C. Y. Chow, H. Ade, D. Pan and H. Yan, *J. Am. Chem. Soc.*, 2017, **139**, 16092–16095.
15   Q. Zhang, X. Xu‡, S. Chen‡, G. B. Bodedla, M. Sun, Q. Hu, Q. Peng, B. Huang, H. Ke, F. Liu, T. P. Russell and X. Zhu, *Sustain. Energy Fuels*, 2018, **2**, 2616–2624.
16   T. A. Welsh, A. Laventure, T. Baumgartner and G. C. Welch, *J. Mater. Chem. C*, 2018, **6**, 2148–2154.
17   T. A. Welsh, A. Laventure, A. F. Alahmadi, G. Zhang, T. Baumgartner, Y. Zou, F. Jäkle and G. C. Welch, *ACS Appl. Energy Mater.*, 2019, **2**, 1229–1240.
18   Z. Luo, T. Liu, Z. Chen, Y. Xiao, G. Zhang, L. Huo, C. Zhong, X. Lu, H. Yan, Y. Sun and C. Yang, *Adv. Sci.*, 2019, **6**, 1802065.

19 J. D. B. Koenig, A. Laventure and G. C. Welch, *ACS Appl. Energy Mater.*, 2019, **2**, 8939–8945.

20 J. R. Cann, C. Cabanetos and G. C. Welch, *ChemPlusChem*, 2017, **82**, 1359–1364.

21 S. M. Barbon and J. B. Gilroy, *Polym. Chem.*, 2016, **7**, 3589–3598.

22 J. S. Dhindsa, R. R. Maar, S. M. Barbon, M. O. Avilés, Z. K. Powell, F. Lagugné-Labarthet and J. B. Gilroy, *Chem. Commun.*, 2018, **54**, 6899–6902.

23 J. S. Dhindsa, A. Melenbacher, S. M. Barbon, M. J. Stillman and J. B. Gilroy, *Dalton Trans.*, , DOI:10.1039/C9DT03417J.

24 R. R. Maar, S. M. Barbon, N. Sharma, H. Groom, L. G. Luyt and J. B. Gilroy, *Chem. – Eur. J.*, 2015, **21**, 15589–15599.

25 R. R. Maar, R. Zhang, D. G. Stephens, Z. Ding and J. B. Gilroy, *Angew. Chem. Int. Ed.*, 2019, **58**, 1052–1056.

26 J. B. Gilroy and E. Otten, *Chem. Soc. Rev.*, 2020, **49**, 85–113.

27 S. M. McAfee, A.-J. Payne, S. V. Dayneko, G. P. Kini, C. E. Song, J.-C. Lee and G. C. Welch, *J. Mater. Chem. A*, 2017, **5**, 16907–16913.

28 S. M. McAfee, A.-J. Payne, A. D. Hendsbee, S. Xu, Y. Zou and G. C. Welch, *Sol. RRL*, 2018, **2**, 1800143.

29 D. Zomerman, J. Kong, S. M. McAfee, G. C. Welch and T. L. Kelly, *ACS Appl. Energy Mater.*, 2018, **1**, 5663–5674.

30 A.-J. Payne, N. A. Rice, S. M. McAfee, S. Li, P. Josse, C. Cabanetos, C. Risko, B. H. Lessard and G. C. Welch, *ACS Appl. Energy Mater.*, 2018, **1**, 4906–4916.

31 A.-J. Payne, S. Li, S. V. Dayneko, C. Risko and G. C. Welch, *Chem. Commun.*, 2017, **53**, 10168–10171.

32 M. E. Farahat, C.-S. Tsao, Y.-C. Huang, S. Hsiung Chang, W. Budiawan, C.-G. Wu and C.-W. Chu, *J. Mater. Chem. A*, 2016, **4**, 7341–7351.

33 T. H. Lee, S. Y. Park, B. Walker, S.-J. Ko, J. Heo, H. Y. Woo, H. Choi and J. Y. Kim, *RSC Adv.*, 2017, **7**, 7476–7482.

34 S. B. Srivastava, S. K. Srivastava and S. P. Singh, *J. Phys. Chem. C*, 2017, **121**, 17104–17111.

35 F. Tintori, A. Laventure and G. C. Welch, *Soft Matter*, 2019, **15**, 5138–5146.

Near-IR Absorption and Photocurrent Generation Using a First-of-Its-Kind Boron Difluoride Formazanate Non-Fullerene Acceptor

(Supporting Information)

Josh D. B. Koenig[a], Mahmoud E. Farahat[a], Jasveer S. Dhindsa[b], Joe B. Gilroy*[b], and Gregory C. Welch*[a]

———

[a] Department of Chemistry, University of Calgary, Calgary, Alberta, Canada T2N 1N4.

[b] Department of Chemistry and the Centre for Advanced Materials and Biomaterials Research (CAMBR), The University of Western Ontario, London, ON, Canada N6A 5B7.

———

* Corresponding Authors:

Email: joe.gilroy@uwo.ca;
Phone Number: 1-519-661-2111 (ext. 81561)

Email: gregory.welch@ucalgary.ca;
Phone number: 1-403-210-7603

———

Keywords: BF_2 formazanate; non-fullerene acceptor; perylene diimide; PDI; Near-IR; OPV

TABLE OF CONTENTS

1. Methods and Materials

Materials: FBT polymer donor: poly[(2,5-bis(2-hexyldecyloxy) phenylene)-alt-(5,6-difluoro-4,7-di(thiophen-2-yl)benzo[c][1,2,5]thiadiazole)] (PPDT2FBT) was purchased from Brilliant Matters. Fullerene acceptor [6,6]-phenyl-C_{61}-butyric acid methyl ester ($PC_{61}BM$) was purchased from Ossila. All other reactants, reagents, and catalysts were purchased from Sigma-Aldrich or VWR and used without further purification.

CHN Elemental Analysis: Elemental analyses were performed by Jian Jun (Johnson) Li in the Chemical Instrumentation Facility at the University of Calgary. A Perkin Elmer 2400 Series II CHN Elemental Analyzer was used to obtain CHN data, using ~1.5 mg of sample (with particle sizes ranging between 0.2 and 0.5 mm in diameter).

Nuclear Magnetic Resonance (NMR): All NMR spectroscopy experiments were recorded using a Bruker Avance III 500 MHz spectrometer. All experiments were performed in tetrachloroethane-d_2. Chemical shifts (referenced to residual solvent) were reported in parts per million (ppm). Multiplicities were reported as follows: singlet (s), doublets (d), triplets (t), quartet (q), pentet (p), doublet of doublets (dd), doublet of triplets (dt), doublet of quartets (dq), triplet of doublets (td), triplet of triplets (tt), and multiplets (m).

High-resolution MALDI-TOF (HR MALDI-TOF): High-resolution MALDI-TOF mass spectrometry measurements were performed by Johnson Li in the Chemical Instrumentation Facility at the University of Calgary. The sample solution (~ 1 µg/mL in dichloromethane) was mixed with matrix trans2-[3-(4-tert-Butylphenyl)-2-methyl-2-propenylidene]malononitrile (DCTB) solution (~5 mg/mL in methanol). All spectra were acquired using a Bruker Autoflex III Smartbeam MALDI-TOF, set to the positive reflective mode (Na:YAG 355 nm laser settings: laser offset = 62-69; laser frequency = 200 Hz; and number of shots = 300). The target used was Bruker MTP 384 ground steel plate target.

UV-Visible Spectroscopy (UV-Vis): All absorption measurements were recorded using Agilent Technologies Cary 60 UV-Vis spectrometer at room temperature. All solution UV-Vis spectra were measured with 2 mm quartz cuvettes, using $CHCl_3$ as solvent. Stock solutions (~1.0 mg/mL) of each compound were prepared, serially diluted to concentrations between 10^{-5} - 10^{-6} M, and then used to construct calibration curves for determining molar absorptivity. Neat films were prepared by spin-coating from a 1 % wt/v solution onto clean Corning glass slides. Prior to use, glass slides were cleaned with soap and water, acetone and isopropanol, and followed by UV/ozone treatment using a Novascan UV/ozone cleaning system.

Photoluminescence (PL): All emission measurements were recorded using an Agilent Technologies Cary Eclipse fluorescence spectrophotometer at room temperature.

Atomic Force Microscopy (AFM): AFM measurements were performed by using a TT2-AFM (AFM Workshop) in tapping mode and WSxM software with an 0.01-0.025 Ohm/cm Sb (n) doped Si probe with a reflective back side aluminum coating. Samples for AFM measurement were the same ones that were used to collect the respective the device parameters.

X-Ray Diffraction (XRD): All X-ray diffraction experiments were performed with a PROTO AXRD Benchtop Powder Diffractometer using θ-2θ scans and Cu K-α radiation

Cyclic Voltammetry (CV): Electrochemical measurements were performed using a CH Instruments Inc. Model 1200B Series Handheld Potentiostat. A standard 3-electrode setup was utilized, consisting of a freshly polished glassy carbon disk working electrode (WE), Pt-wire counter electrode (CE), and Ag-wire pseudo-reference electrode (RE). All measurements were referenced to ferrocene ($Fc^{+/0}$) as internal standard. All cyclic voltammetry experiments were performed at a scan rate of 100 mV/s. Sample solutions, with 1 mM compound and 0.1 M tetrabutylammonium hexafluorophosphate ($TBAPF_6$) supporting electrolyte, were prepared in anhydrous CH_2Cl_2. All electrochemical solutions were sparged with dry gas (either N_2 or argon) for 5 minutes to deoxygenate the system prior to measurements. The ionization potentials (IP) and electron affinities (EA) were estimated by correlating the 1st oxidation and 1st reduction potentials (E_p ox $Fc^{0/+}$, $E_{1/2}$ red $Fc^{0/+}$) to the normal hydrogen electrode (NHE), assuming the IP of $Fc^{0/+}$ to be 4.80 eV, respectively.[1]

Power Conversion Efficiency (PCE) and External Quantum Efficiency (EQE): The current density-voltage (J-V) curves were measured by a Keithley 2420 source measure unit. The photocurrent was measured under AM 1.5 illumination at 100 mW/cm^2 under a Solar Simulator (Newport 92251A-1000). The standard silicon solar cell (Newport 91150V) was used to calibrate light intensity. EQE was measured in a QEX7 Solar Cell Spectral Response/QE/IPCE Measurement System (PV Measurement, Model QEX7, USA) with an optical lens to focus the light into an area about 0.04 cm^2, smaller than the dot cell. The silicon photodiode was used to calibrate the EQE measurement system in the wavelength range from 300 to 1100 nm.

Organic Photovoltaic (OPV) Devices: Inverted device architecture (ITO/ZnO/Ternary Active Layer/MoOx/Ag) was used in OPVs device fabrication. Devices were fabricated using ITO-coated glass substrates cleaned by sequentially ultra-sonicating with detergent and de-ionized water, acetone, and isopropanol followed by exposure to UV/ozone for 30 min. ZnO was subsequently deposited as a sol-gel precursor solution in a N_2 purge box following the method of Sun *et al.*[2] The ternary blend FBT: BF_2PDI_2: $PC_{61}BM$ was dissolved in dichlorobenzene at 1:1:0.5 weight ratio (total concentration of 10 mg/mL) and processed in air at room temperatures. The substrates with the cast active layers were kept in an N_2 atmosphere glovebox overnight before evaporating MoO_3 and Ag. The 10 nm of MoO_3 followed by 100 nm of Ag were thermally deposited under vacuum (10^{-5} Torr). Active areas of the devices were 0.14 cm^2.

Computational Details: Gas-phase B3LYP/6-31G(d,p) ground-state equilibrium geometry optimizations were considered within Gaussian 09.[3] To reduce the computational cost, all alkyl-substituents were truncated to methyl groups. Molecular dihedral angles were systematically altered to ensure that the optimized geometric lower energy minimum was not missed structure possessed no imaginary frequencies . The resulting structure was characterized through frequency calculations (at the same level of theory). TD-SCF calculations were also performed from this optimized geometry. Single point calculations were performed on this structure to generate molecular orbitals and electrostatic potential maps.

2. Synthetic/Experimental Procedures

Boron Difluoride Formazanate (EthylHexyl-N-annulated Perylene Diimide)₂ (BF₂PDI₂)

Starting materials 2,6-bis(4-ethynylphenyl)-4-phenyl-1-BF₂-formazanate (BF₂Ace₂) and ethylhexyl-N-annulated Perylene Diimide Bromide (EH-NPDI-Br) were prepared following known literature preparations.[4,5]
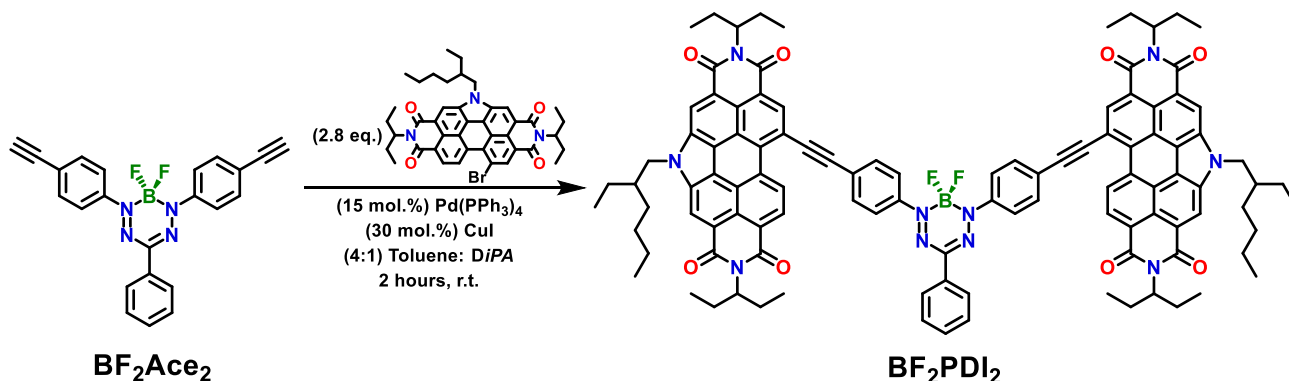
EH-N-PDI-Br (103 mg, 0.14 mmol, 2.8 eq.), BF₂(Ace)₂ (19.9 mg, 0.05 mmol, 1.0 eq.), and CuI (2.8 mg, 0.015 mmol, 30 mol %) were combined into a 10 mL μwave vial. The vial was brought into the glovebox, Pd(PPh₃)₄ (8.7 mg, 0.008 mmol, 15 mol %) was added, and then the vial was sealed. A degassed mixture of toluene:diisopropylamine (4:1) was transferred into the vial using a Cannula line. The reaction mixture was stirred at room temperature for 2 hrs (monitoring reaction progress by TLC) and then subsequently quenched by pouring into H₂O (50 mL). The resulting solution was liquid-liquid extracted using CH₂Cl₂ (3 x 25 mL). The organic extracts were dried over Na₂SO₄ and then filtered through a short Celite plug. Organic solvent was removed by rotary evaporation and the resulting crude solid was purified by silica-gel column chromatography (eluting with CH₂Cl₂). The purified purple solid was precipitated into MeOH and collected by vacuum filtration (59 mg, 0.035 mmol, <u>69%</u>).

<u>¹H NMR</u> (500 MHz, Tetrachloroethane-d₂) δ 9.67 (d, J = 8.3 Hz, 2H), 8.46 (s, 2H), 8.41 (s, 4H), 8.34 (d, J = 8.3 Hz, 2H), 7.58 (dd, J = 19.5, 7.6 Hz, 5H), 7.35 (d, J = 8.4 Hz, 4H), 6.99 – 6.88 (m, 4H), 4.59 – 4.51 (m, 4H), 4.15 (t, J = 8.1 Hz, 4H), 1.45 – 1.26 (m, 8H), 0.94 – 0.55 (m, 22H), 0.39 – 0.25 (m, 24H), 0.22 (t, J = 7.3 Hz, 6H).

<u>¹³C{¹H} NMR</u> (126 MHz, Tetrachloroethane-d₂) δ 134.38, 132.01, 131.59, 130.82, 127.97, 126.06, 123.35, 122.97, 122.68, 121.37, 121.21, 119.03, 118.38, 118.23, 116.15, 109.40, 98.35, 78.70, 78.56, 78.48, 78.25, 73.03, 56.64, 40.27, 29.59, 27.35, 24.12, 23.03, 21.99, 12.99, 10.51, 10.50, 9.56. *quaternary centres were not observed due to limited solubility of BF₂PDI₂*
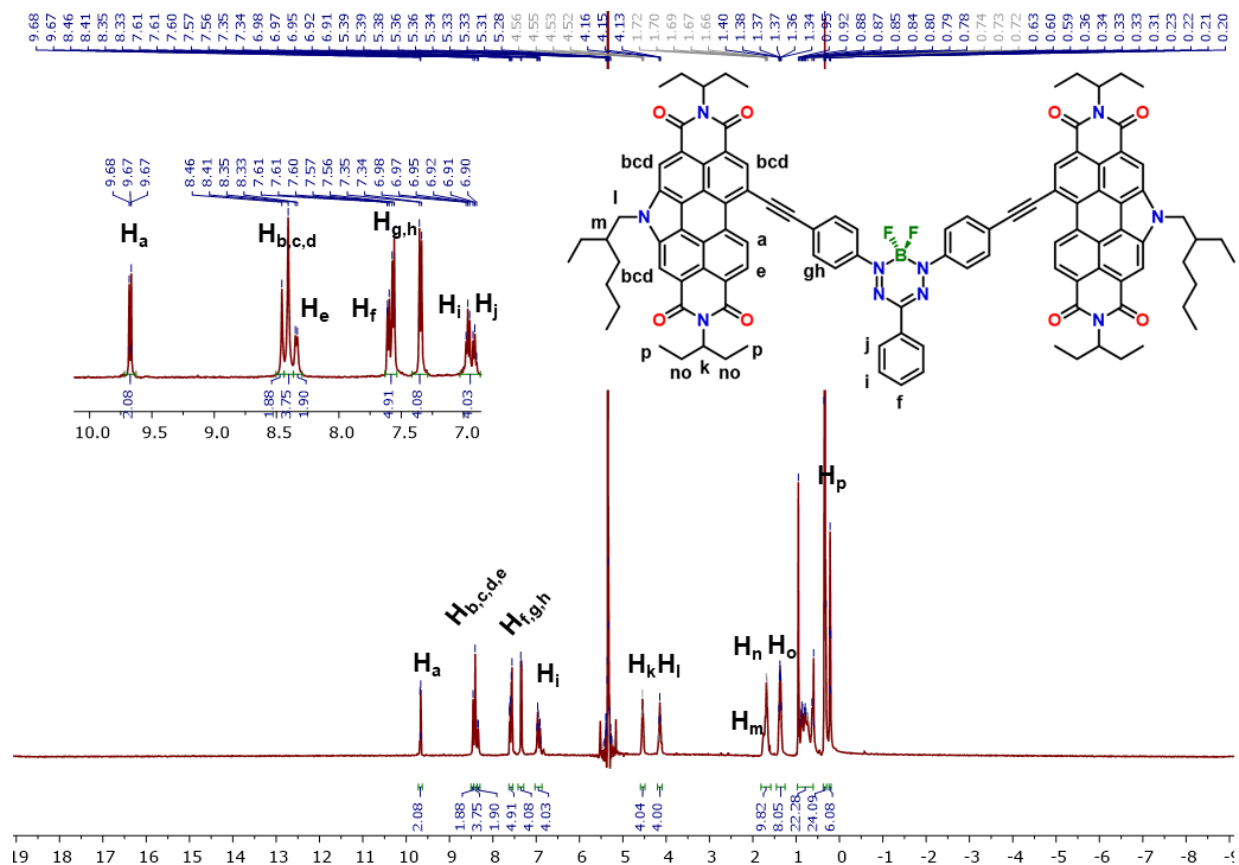
<u>¹¹B NMR</u> (161 MHz, Tetrachloroethane-d_2) δ -0.47 (t, $^1J_{BF}$ = 28.9 Hz, 1B).

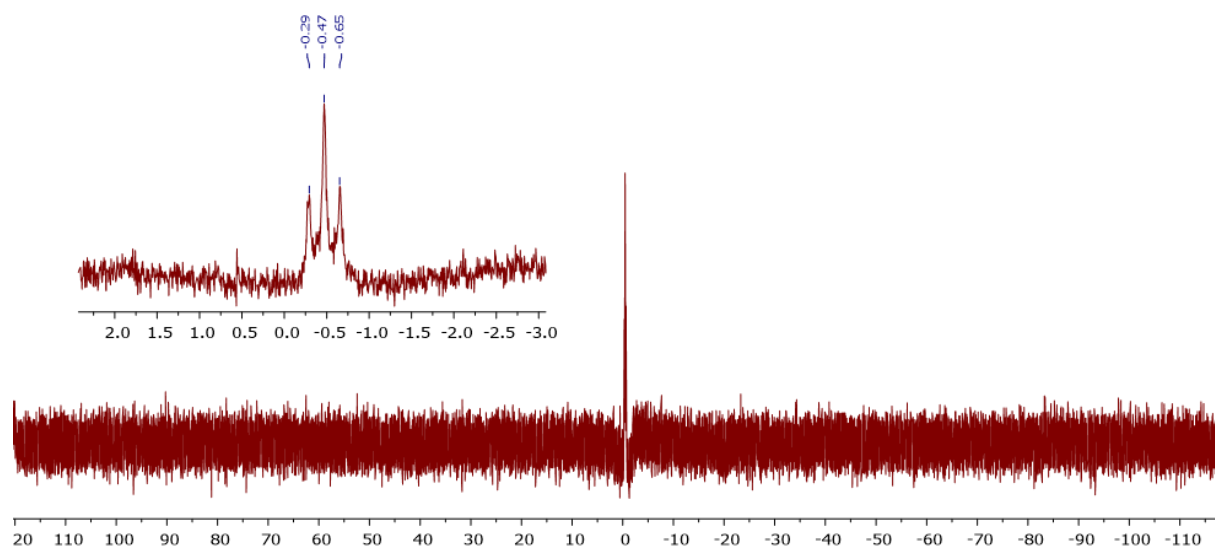<u>¹⁹F NMR</u> (471 MHz, Tetrachloroethane-d_2) δ -143.24 (q, $^1J_{FB}$ = 28.4 Hz, 2F).

<u>HRMS</u> ([M-H]⁺) calculated for M = C₁₀₇H₁₀₁N₁₀O₈BF₂: 1701.7786; detected [M-H]⁺: 1701.7720.

<u>CHN</u> theoretical (%) C: 75.43, H: 5.98, N: 8.22; found (%) C: 74.74; H: 6.02; N: 7.94.

3. NMR Spectra
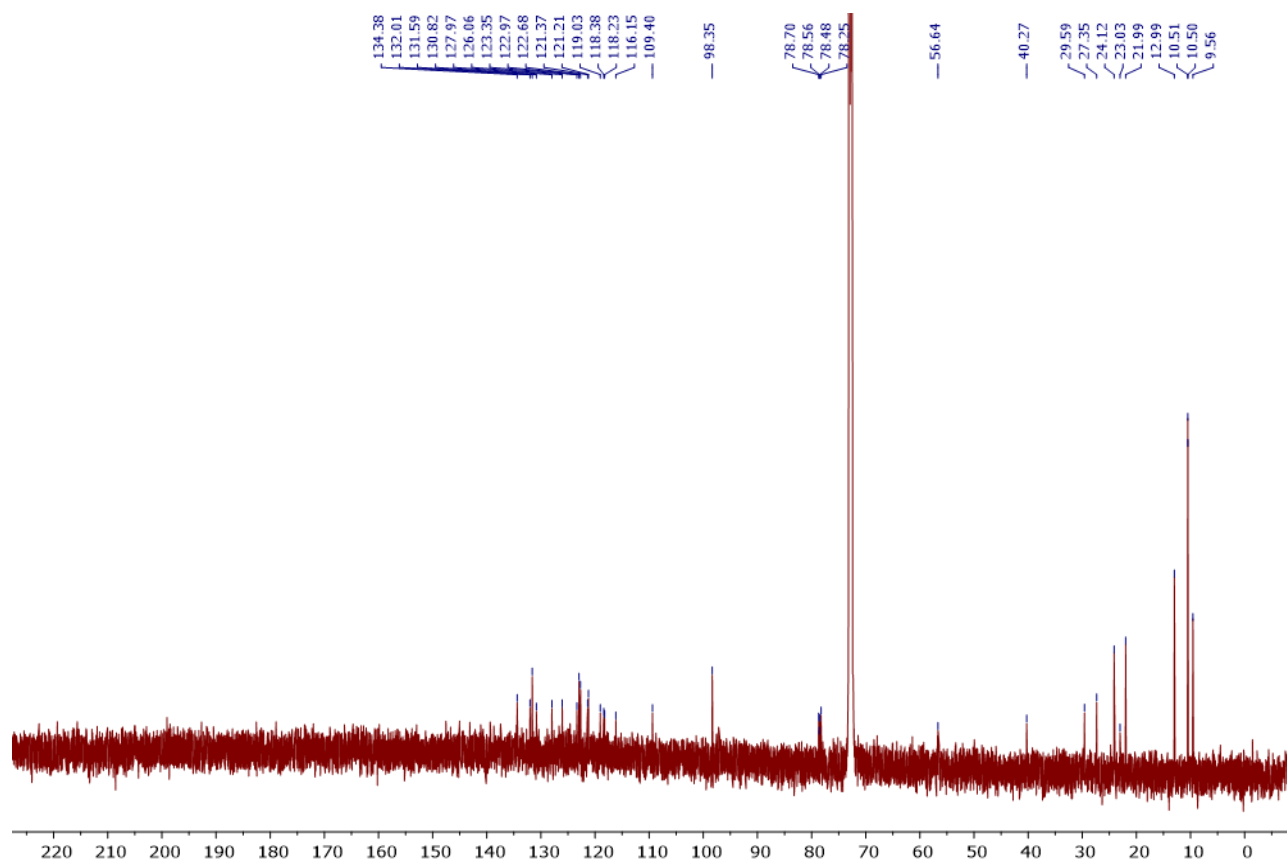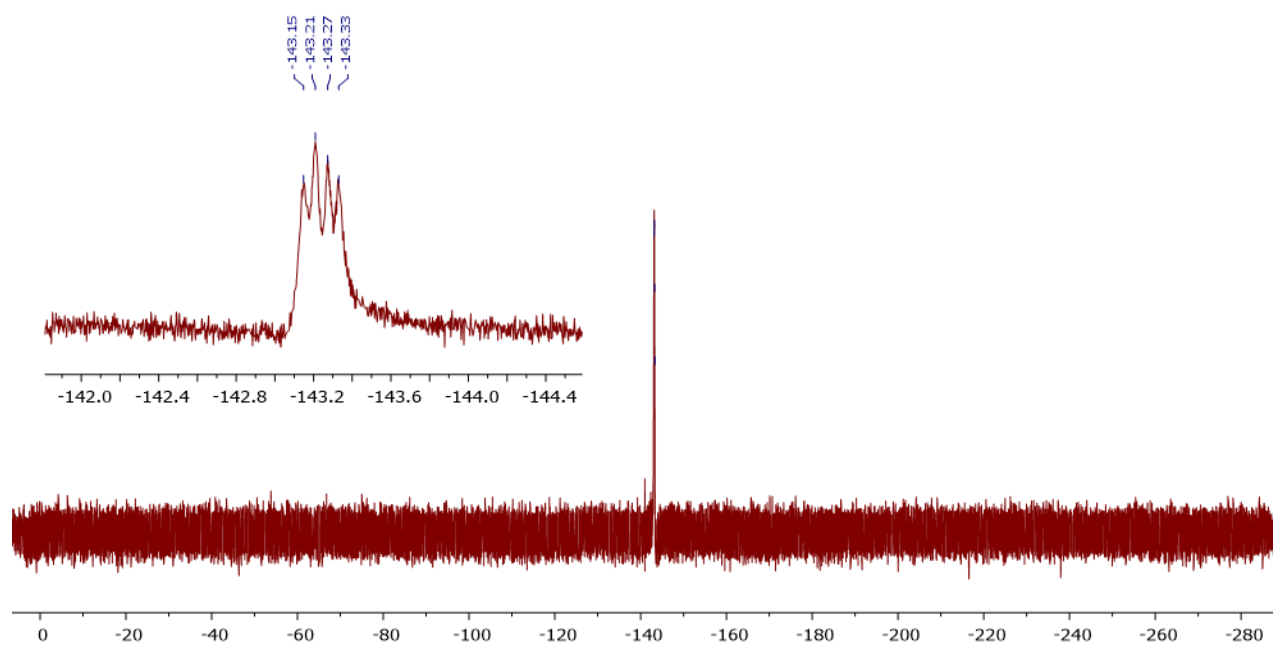

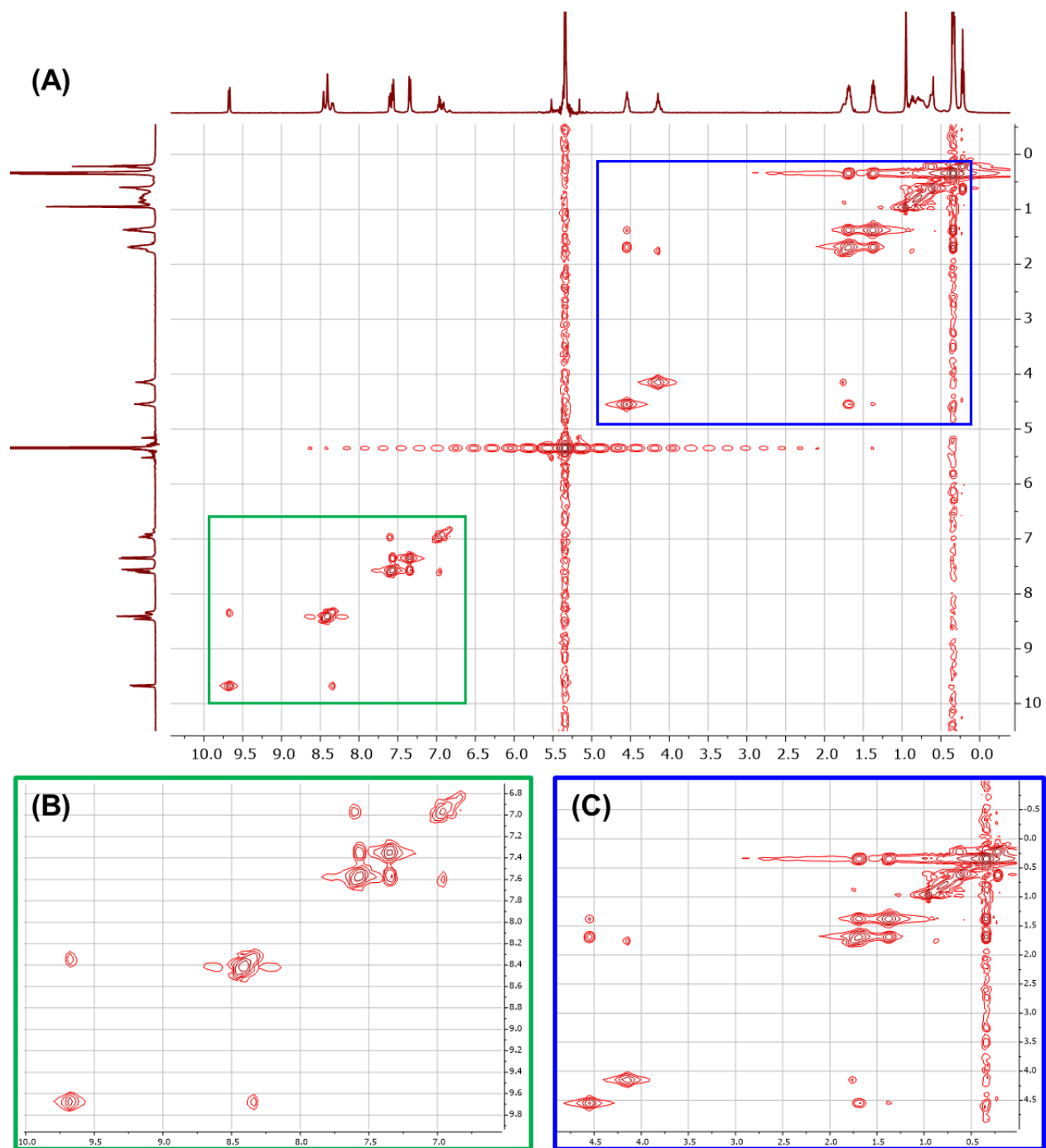**Fig. S1** ^{1}H NMR spectrum of BF$_2$PDI$_2$ (500 MHz, Tetrachloroethane-d$_2$).

Fig. S2 ^{11}B NMR spectrum of BF$_2$PDI$_2$ (161 MHz, Tetrachloroethane-d$_2$).

Fig. S3 $^{13}C\{^1H\}$ NMR spectrum of BF$_2$PDI$_2$ (126 MHz, Tetrachloroethane-d$_2$).

Fig. S4 ^{19}F NMR spectrum of BF$_2$ PDI$_2$ (471 MHz, Tetrachloroethane-d$_2$).

Fig. S5 ^{1}H-^{1}H COSY spectrum (A) of BF$_2$PDI$_2$ (500 MHz, Tetrachloroethane-d$_2$) with enhanced views of the aromatic (B) and aliphatic (C) regions.

4. MS, CHN EA, & Thermal Properties
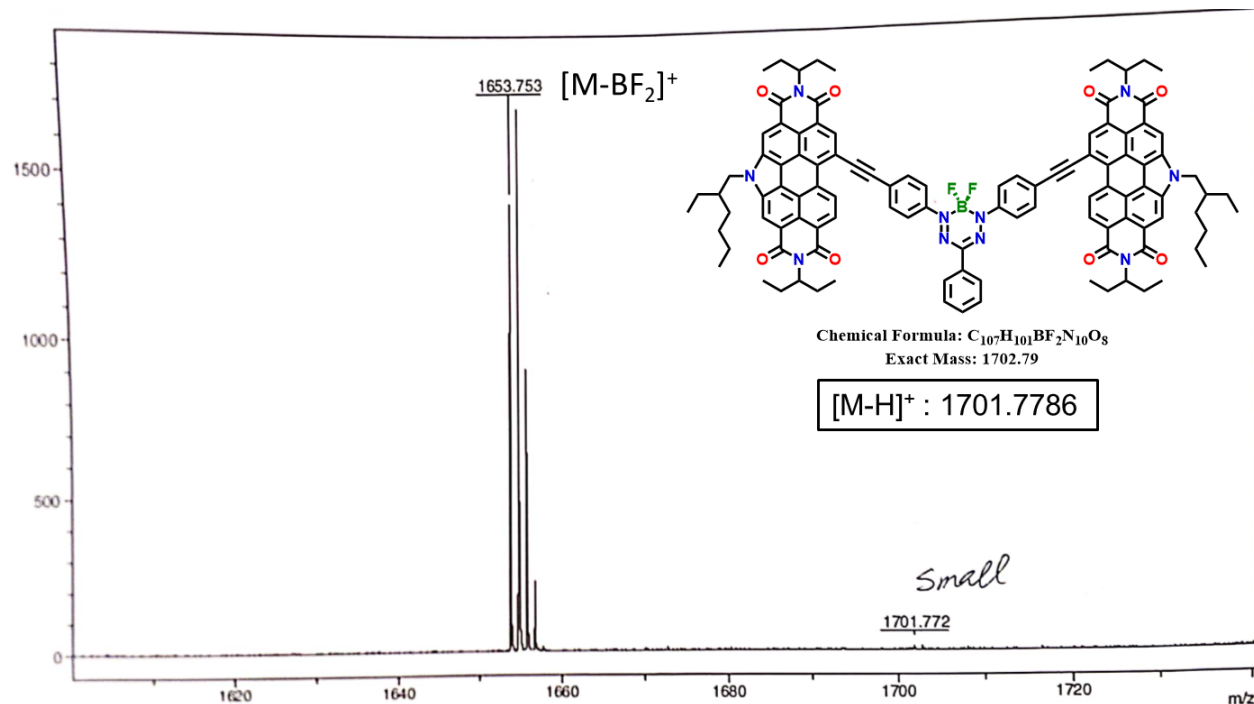
Fig. S6 HR MADLI TOF mass spectrum of BF_2PDI_2.

University of Calgary
Department of Chemistry EA   Date: 2/5/2020

Name:	JOSH	Group:	GW
Sample:	BF_2PDI_2	Weight (mg):	1.59
%C (Actual):	74.74	%C (Theorectical):	75.43
%H (Actual):	6.02	%H (Theoretical):	5.98
%N (Actual):	7.94	%N (Theoretical):	8.22

Fig. S7 CHN elemental analysis of BF_2PDI_2.
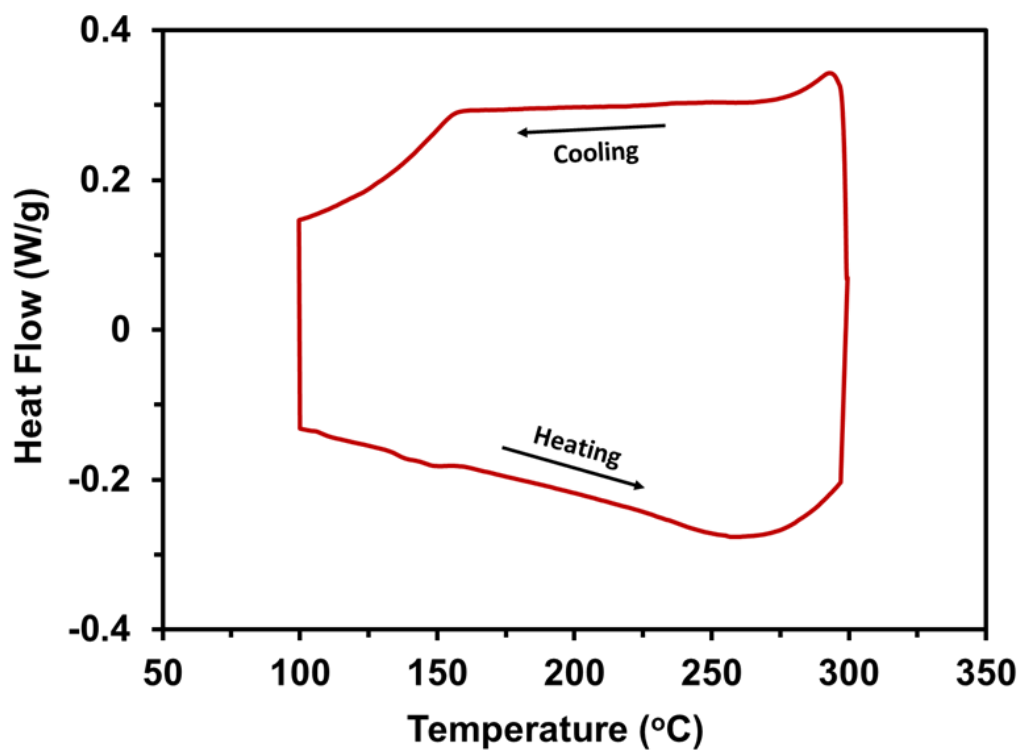
Fig. S8 Differential scanning calorimetry profile of BF_2PDI_2.
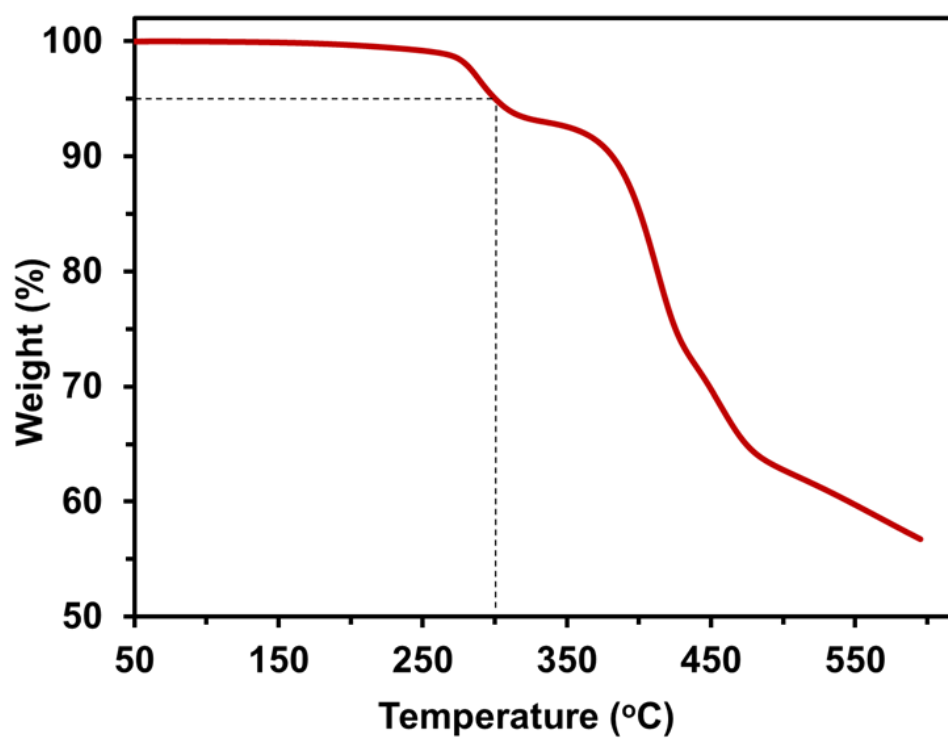
Fig. S9 Thermal gravimetric analysis profile of BF_2PDI_2.
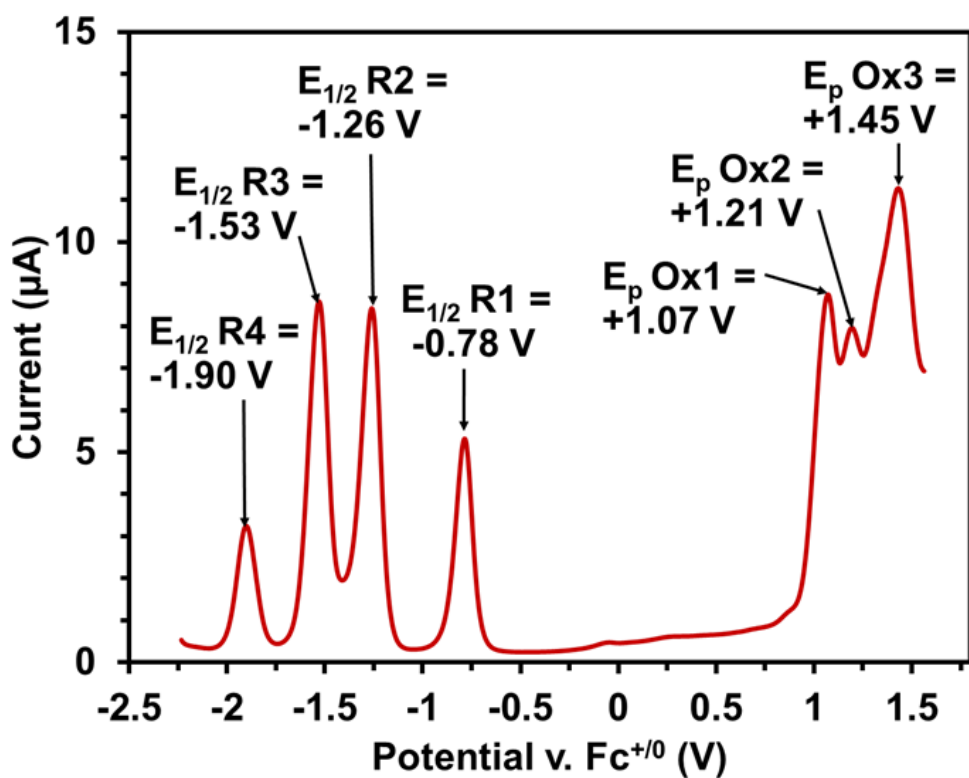
5. UV-Visible Spectroscopy
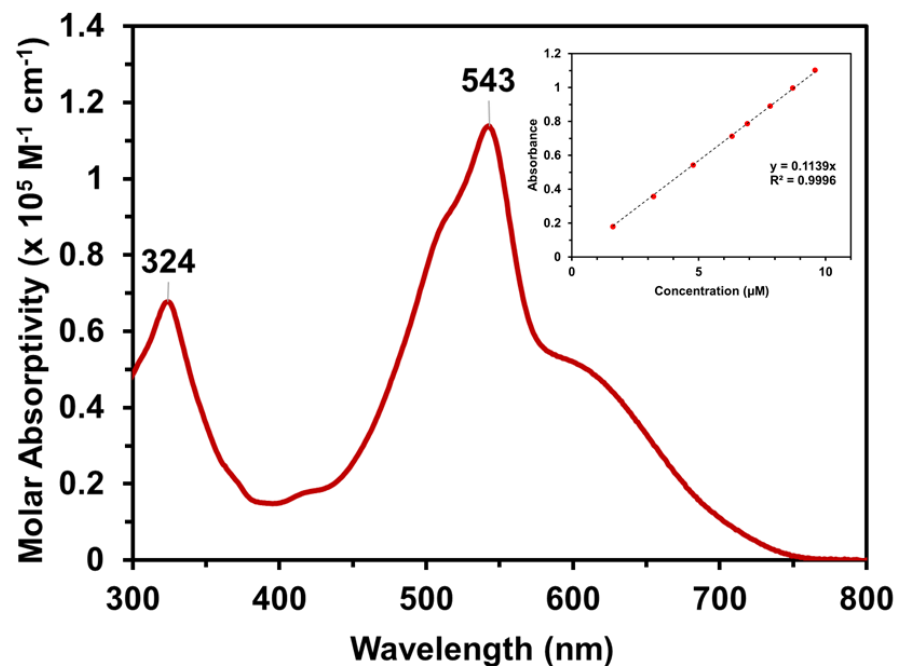
Fig. S10 UV-visible absorption spectrum of BF_2PDI_2 in $CHCl_3$, with calibration curve inset.
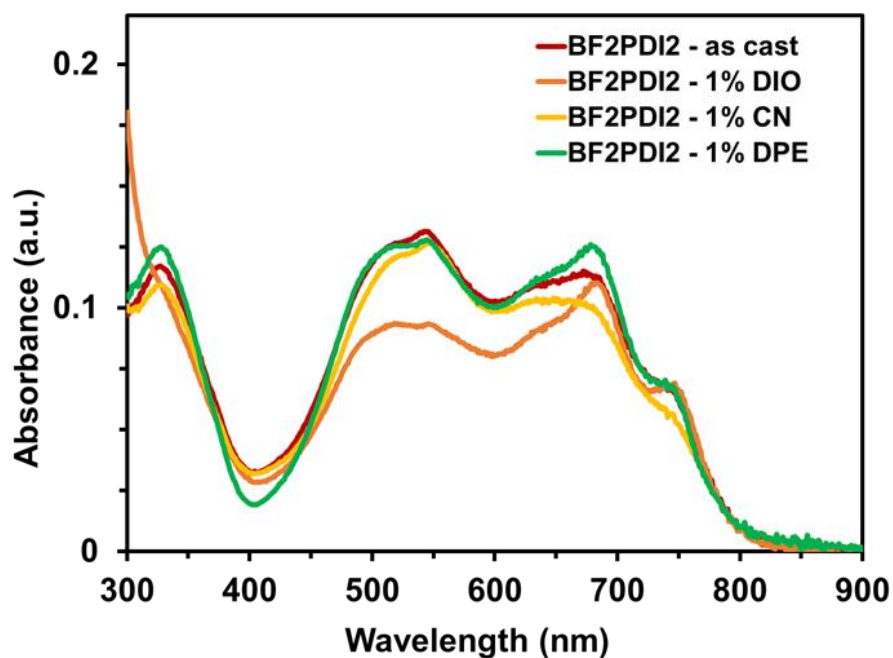

Fig. S11 Comparing the influence of solvent additives 1,8-diiodooctane (DIO), 1-chloronaphthalene (CN), and diphenyl ether (DPE) on the thin film UV-vis absorption spectra of BF_2PDI_2 (spin-coated from 10 mg/mL *o*-DCB solutions).
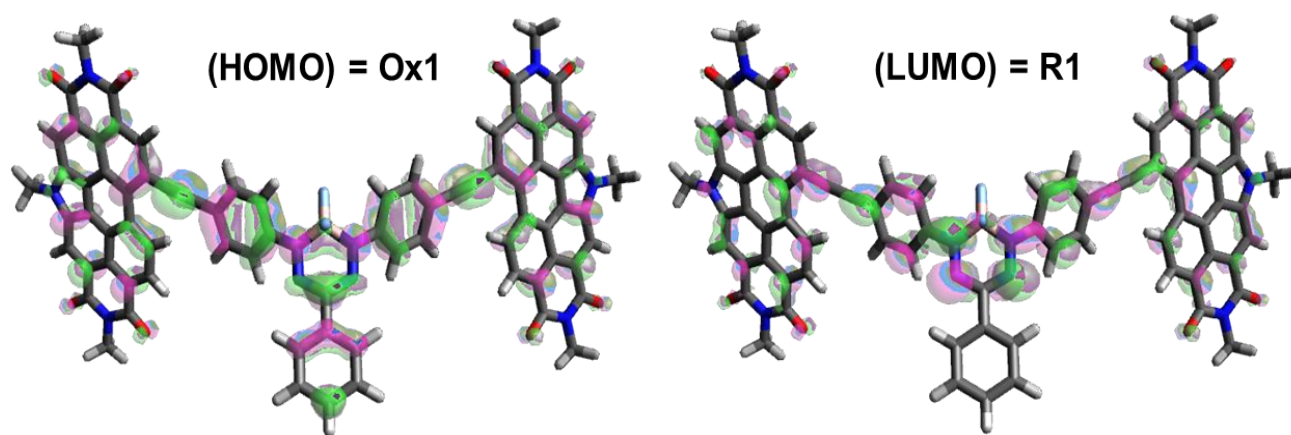
6. Electrochemistry

Fig. S12 Differential pulse voltammogram of BF$_2$PDI$_2$, measured in CH$_2$Cl$_2$ under argon with 0.1 M TBAPF$_6$ supporting electrolyte (WE = glassy carbon, CE = Pt-wire, *pseudo*-RE = Ag/AgCl).
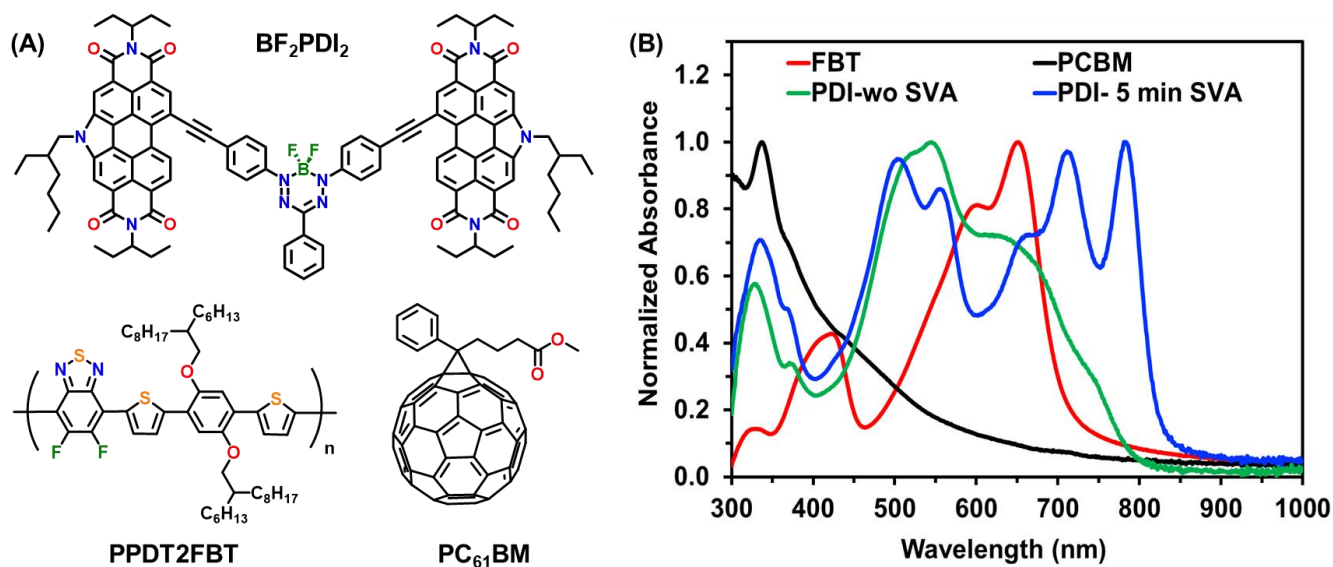
7. Density Functional Theory
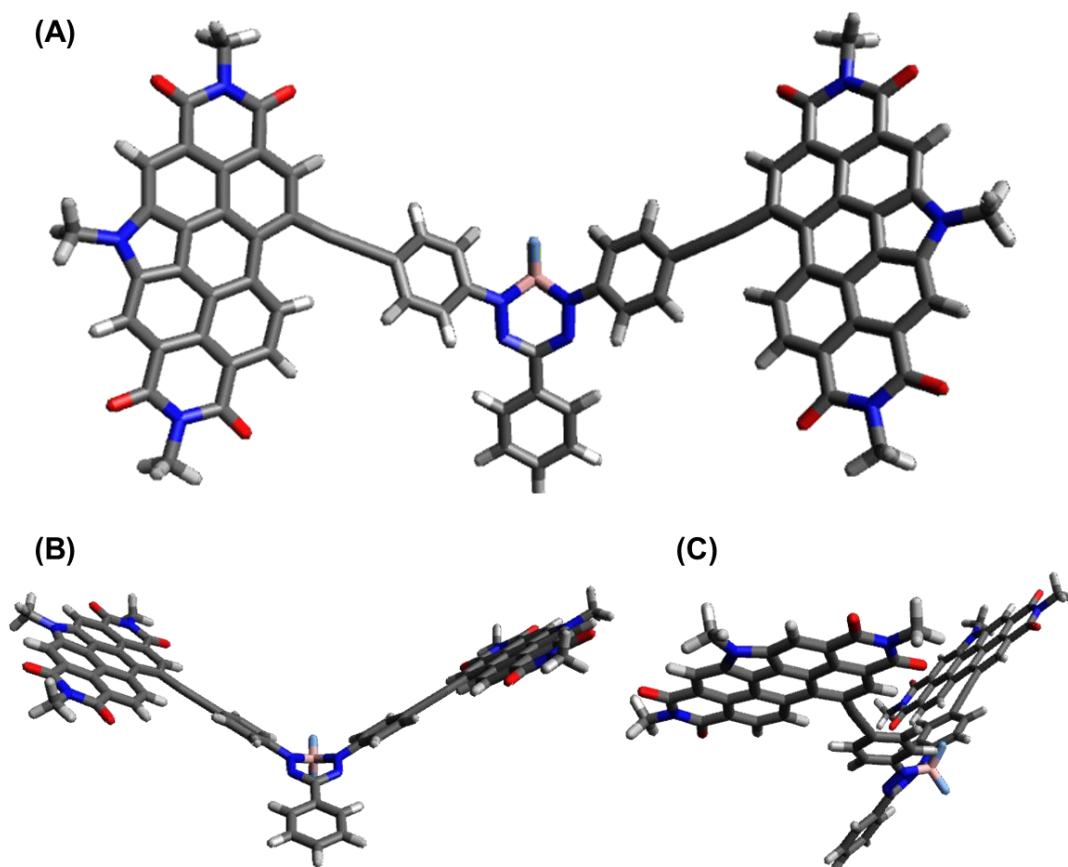
Fig. S13 Optimized geometry for BF_2PDI_2 at B3LYP/6-31G(d,p) ground-state.

Fig. S14 Highest occupied molecular orbital (HOMO) and the lowest unoccupied molecular orbital (LUMO) for BF_2PDI_2 at B3LYP/6-31G(d,p) ground-state.

8. OPV Device Data

Fig. S15 Chemical structures (A) and film optical absorption profiles (B) of all components used in the OPV ternary blend active layer. PDI = BF$_2$PDI$_2$, PCBM = PC$_{61}$BM, FBT = PPDT2FBT in the plot. SVA = solvent vapour annealing for 5 min using CHCl$_3$.

Table S1 Photovoltaic parameters of the devices based on ternary blend (PPDT2FBT: BF$_2$PDI$_2$: PC$_{61}$BM). Metrics corresponding to the devices with the average PCE are in parenthesis.

| PPDT2FBT: BF$_2$PDI$_2$: PC$_{61}$BM	V_{oc} (V)	J_{sc} (mA/cm^2)	FF%	PCE%
As-cast (1:1:0.5, 10 mg/mL)	0.69 (0.69)	1.10 (1.02)	41.3 (40.1)	0.31 (0.28)
5 min SVA (1:1:0.5, 10 mg/mL)	0.64 (0.65)	1.95 (1.84)	48.6 (47.8)	0.61 (0.57)
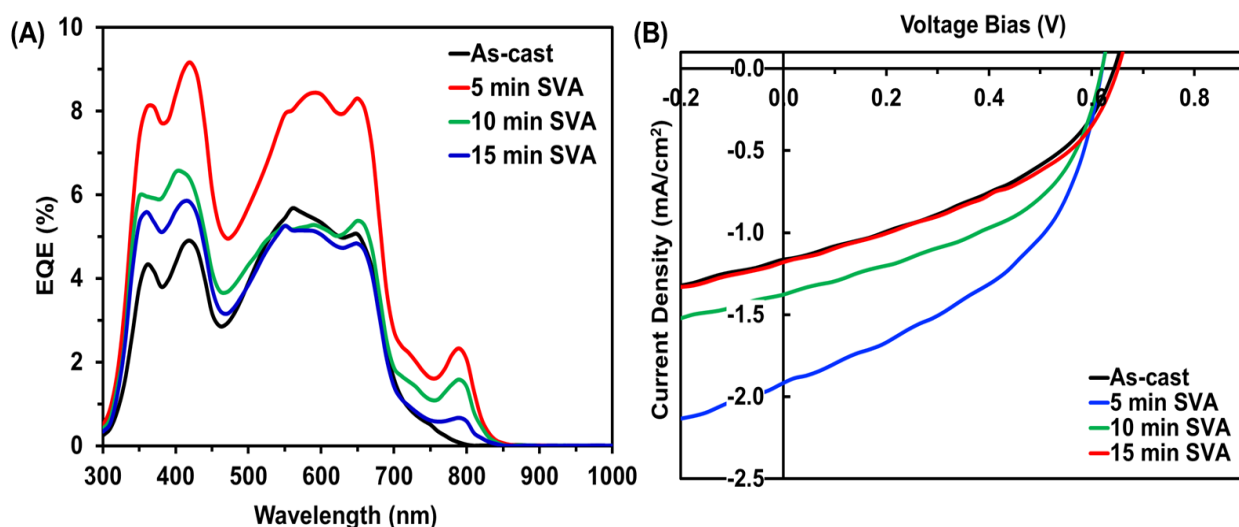
Fig. S16 External quantum efficiency plots (A) and J-V curves (B) comparing the effects of solvent vapor annealing duration on ternary blend OPV devices with PPDT2FBT: BF_2PDI_2: $PC_{61}BM$ (1:1:0.5) active layer at 10 mg/mL total concentration.

Table S2 Photovoltaic parameters of the devices based on ternary blend (PPDT2FBT: BF_2PDI_2: $PC_{61}BM$), comparing the effects of SVA treatment duration.

| PPDT2FBT: BF_2PDI_2: $PC_{61}BM$	V_{oc} (V)	J_{sc} (mA/cm^2)	FF (%)	PCE (%)
As-cast (1:1:0.5, 10 mg/mL)	0.64	1.17	41	0.31
5 min SVA (1:1:0.5, 10 mg/mL)	0.62	1.91	45	0.53
10 min SVA (1:1:0.5, 10 mg/mL)	0.62	1.37	47	0.41
15 min SVA (1:1:0.5, 10 mg/mL)	0.65	1.18	41	0.32
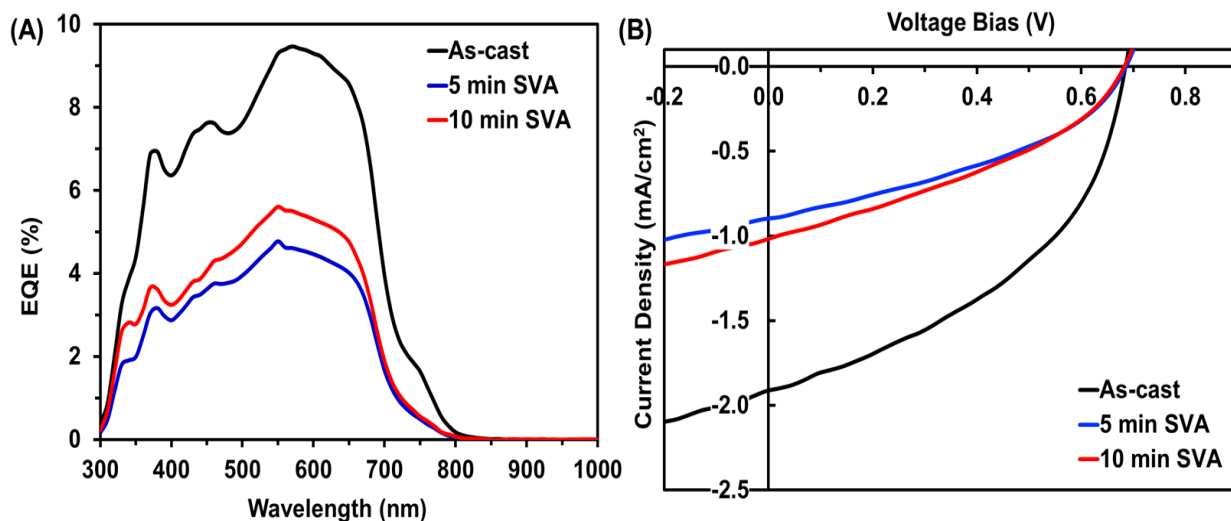
Fig. S17 External quantum efficiency plots (A) and J-V curves (B) comparing the effects of solvent vapor annealing duration on ternary blend OPV devices with PPDT2FBT: BF_2PDI_2: $PC_{61}BM$ (1:0.75:0.75) active layer at 20 mg/mL total concentration.

Table S3 Photovoltaic parameters of the devices based on ternary blend (PPDT2FBT: BF_2PDI_2: $PC_{61}BM$), comparing the effects of solvent vapor annealing on an altered the ternary blend.

PPDT2FBT: BF_2PDI_2: $PC_{61}BM$	*V_{oc} (V)*	*J_{sc} (mA/cm²)*	*FF (%)*	*PCE (%)*
As-cast (1:0.75:0.75, 20 mg/mL)	0.68	1.91	44	0.58
5 min SVA (1:0.75:0.75, 20 mg/mL)	0.68	0.90	39	0.24
10 min SVA (1:0.75:0.75, 20 mg/mL)	0.68	1.01	36	0.25
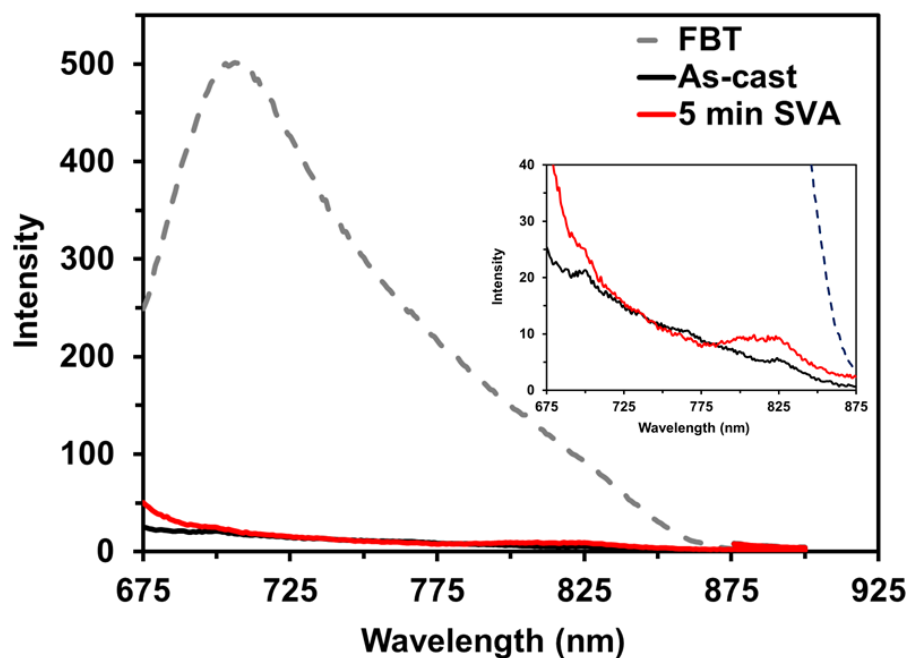
Fig. S18 Photoluminescence spectra of OPV devices with PPDT2FBT: BF_2PDI_2: $PC_{61}BM$ (1:1:0.5) active layer at 10 mg/mL total concentration, before (black) and after (red) solvent vapor annealing from $CHCl_3$. The excitation wavelength was 651 nm.
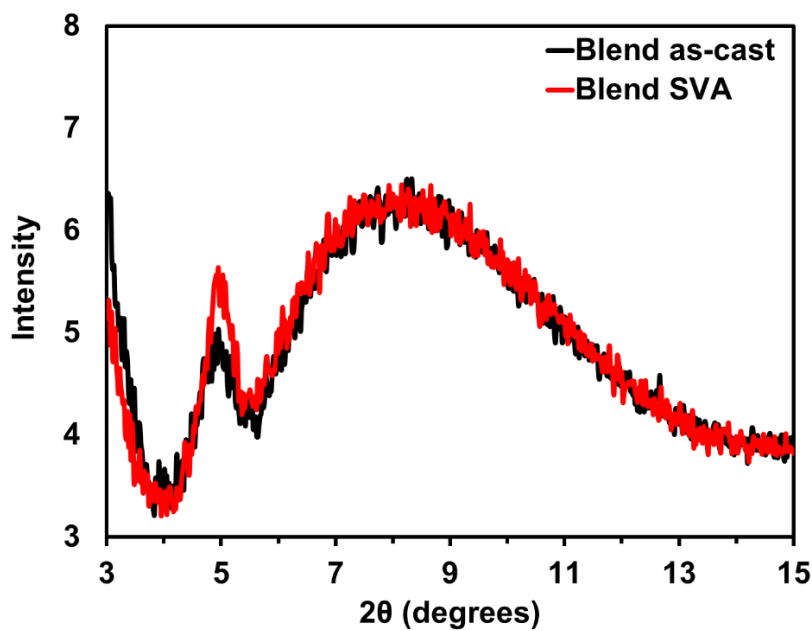
Fig. S19 X-ray diffraction spectra of spin-cast PPDT2FBT: BF_2PDI_2: $PC_{61}BM$ (1:1:0.5), before (black) and after (red) solvent vapor annealing from $CHCl_3$.

9. References

1 J. Pommerehne, H. Vestweber, W. Guss, R. F. Mahrt, H. Bässler, M. Porsch and J. Daub, *Adv. Mater.*, 1995, **7**, 551–554.

2 Y. Sun, J. H. Seo, C. J. Takacs, J. Seifter and A. J. Heeger, *Adv. Mater.*, 2011, **23**, 1679–1683.

3 Frisch, M. J.; Trucks, G. W.; Schlegel, H. B.; Scuseria, G. E.; Robb, M. A.; Cheeseman, J. R.; Scalmani, G.; Barone, V.; Petersson, G. A.; Nakatsuji, H.; Li, X.; Caricato, M.; Marenich, A. V.; Bloino, J.; Janesko, B. G.; Gomperts, R.; Mennucci, B.; Hratchian, H. P.; Ortiz, J. V.; Izmaylov, A. F.; Sonnenberg, J. L.; Williams-Young, D.; Ding, F.; Lipparini, F.; Egidi, F.; Goings, J.; Peng, B.; Petrone, A.; Henderson, T.; Ranasinghe, D.; Zakrzewski, V. G.; Gao, J.; Rega, N.; Zheng, G.; Liang, W.; Hada, M.; Ehara, M.; Toyota, K.; Fukuda, R.; Hasegawa, J.; Ishida, M.; Nakajima, T.; Honda, Y.; Kitao, O.; Nakai, H.; Vreven, T.; Throssell, K.; Montgomery, J. A., Jr.; Peralta, J. E.; Ogliaro, F.; Bearpark, M. J.; Heyd, J. J.; Brothers, E. N.; Kudin, K. N.; Staroverov, V. N.; Keith, T. A.; Kobayashi, R.; Normand, J.; Raghavachari, K.; Rendell, A. P.; Burant, J. C.; Iyengar, S. S.; Tomasi, J.; Cossi, M.; Millam, J. M.; Klene, M.; Adamo, C.; Cammi, R.; Ochterski, J. W.; Martin, R. L.; Morokuma, K.; Farkas, O.; Foresman, J. B.; Fox, D. J Gaussian 09 Revis. E01 Gaussian Inc Wallingford CT.

4 S. M. Barbon and J. B. Gilroy, *Polym. Chem.*, 2016, **7**, 3589–3598.

5 A. D. Hendsbee, J.-P. Sun, W. K. Law, H. Yan, I. G. Hill, D. M. Spasyuk and G. C. Welch, *Chem. Mater.*, 2016, **28**, 7098–7109.